Journal of Materials Chemistry A

PAPER

Cite this: J. Mater. Chem. A, 2016, 4, 15861

Electrospun nanofiber-supported carbon aerogel as a versatile platform toward asymmetric supercapacitors†

Feili Lai,[a] Yunpeng Huang,[a] Lizeng Zuo,[a] Huahao Gu,[a] Yue-E Miao*[b] and Tianxi Liu*[ab]

Received 8th June 2016
Accepted 21st August 2016

DOI: 10.1039/c6ta04797a

www.rsc.org/MaterialsA

As a novel kind of carbon-based material, carbon aerogels have attracted widespread attention owing to their integrated properties of a large internal surface area, small pore size, and outstanding mechanical strength. In this study, a fascinating carbon aerogel has been rationally designed with a unique cellular structure, consisting of one-dimensional carbon nanofibers derived from oxidized polyacrylonitrile (o-PAN) and two-dimensional carbon sheets originating from polyimide (PI). The interconnected o-PAN/PI (oPP) carbon aerogel exhibits low density but increased mechanical strength and can not only act as a versatile adsorbent but also as an ideal template for the *in situ* growth of MnO_2 nanosheets to obtain oPP@MnO_2 hybrid carbon aerogel. The oPP@MnO_2 composite aerogel exhibits extraordinary electrochemical characteristics with a maximum specific capacitance of 1066 F g^{-1}, approaching the theoretical value (1370 F g^{-1}) of MnO_2. Moreover, an assembled oPP@MnO_2//activated oPP (A-oPP) asymmetric supercapacitor delivers a considerably high energy density of up to 30.3 W h kg^{-1}, highlighting the advantages of the unique cellular structure of the oPP carbon aerogel and oPP@MnO_2 hybrid carbon aerogel. Therefore, the successful fabrication of the oPP carbon aerogel widens the scope of traditional electrospun lamellar membranes to multi-dimensional aerogels, providing a new strategy for the construction of nanofiber-based materials for energy storage and environmental protection applications.

Introduction

As a family of three-dimensional (3D) porous materials, carbon aerogels are characterized by low density, large internal surface area, and large pore volume, and have been promising candidates for various applications in the fields of insulating materials, hydrogen storage, catalyst supports, adsorbents, and energy storage.[1–3] In particular, their 3D interconnected network with an open porous structure greatly facilitates the penetration of guest molecules/ions into the interior space, which makes carbon aerogels attractive candidates for potential applications in the fields of environmental remediation and energy storage/conversion.[4,5] In general, three main approaches are adopted during the fabrication of carbon aerogels, including the direct carbonization of organogels, self-assembly of nanocarbon building blocks (such as carbon nanotubes or graphene sheets), and chemical vapor deposition. However, the inevitable drawbacks of the use of toxic and expensive precursors, the requirement for complex equipment and technology, and low production ability, severely hinder the further practical development of carbon aerogels.[6–9] Therefore, it is highly desirable to develop simple and environmentally friendly synthesis methods for preparing structurally defined carbon aerogels with precisely controlled morphologies and compositions toward large-scale production.

Notably, owing to their controllable diameter, large specific surface area, high porosity and facile preparation process, nanofibers obtained by electrospinning are considered to be ideal one-dimensional building blocks for the construction of macroscopic fibrous aerogels to overcome the aforementioned drawbacks of existing carbon aerogels.[10–12] With tunable densities and shapes, robust bulk aerogels can be easily generated by the reconstruction of traditional electrospun nanofiber membranes from various selective raw materials such as polymers, ceramics, metals and carbons.[13,14] For example, a three-dimensionally crosslinked nanofibrous aerogel has been reconstructed from the double components of polyacrylonitrile/bifunctional benzoxazine nanofibers and silicon dioxide nanofibers by means of the dual processes of

[a]State Key Laboratory of Molecular Engineering of Polymers, Department of Macromolecular Science, Fudan University, Shanghai 200433, China. E-mail: txliu@fudan.edu.cn

[b]State Key Laboratory for Modification of Chemical Fibers and Polymer Materials, College of Materials Science and Engineering, Donghua University, Shanghai 201620, China. E-mail: txliu@dhu.edu.cn; yuee_miao@dhu.edu.cn

† Electronic supplementary information (ESI) available: SEM, TEM, XPS, XRD, EDS, TGA, adsorptive properties of carbon aerogels, and electrochemical properties of electrode materials and asymmetric supercapacitors are elucidated. See DOI: 10.1039/c6ta04797a

electrospinning and a freeze-shaping technique.[15] The nanofibrous aerogel exhibits an ultralow density of 0.12 mg cm^{-3} and rapid recovery from deformation, as well as efficient energy absorption properties for a wide range of potential applications in the fields of thermal insulation, sound absorption, emulsion separation and electric conduction that is responsive to elasticity. However, the absence of a strong framework support in the interior structure of fibrous aerogels leads to their poor stress tolerance under harsh conditions. Inspired by the bottom-up self-assembly of polymer precursors with excellent thermal stability, which readily results in stable lamellar structures and spherulites *via* the careful selection of monomers or polymerization conditions, polymer self-assembly has been proved to be an effective strategy for introducing strong chemical/physical bonds between electrospun nanofibers, thus producing highly crosslinked 3D structures of fibrous aerogels with optimized mechanical properties, as well as facilitating the penetration of guest molecules/ions.

In particular, the precursor of polyimide (PI), poly(amide acid) (PAA), has been found to bond easily with electrospun nanofibers for the integrated formation of fibrous aerogels, which is attributed to its enrichment in hydrophilic groups (*e.g.*, –COOH and –OH). Furthermore, owing to its diverse aromatic molecular structures, polyimide possesses excellent mechanical strength, which makes it a promising precursor for the fabrication of carbon aerogels with a high carbon yield and good mechanical properties. Here, an innovative carbon aerogel consisting of one-dimensional carbon nanofibers and two-dimensional carbon sheets has been successfully constructed *via* electrospinning, freeze-shaping and carbonization processes. Benefiting from the efficient binding between oxidized polyacrylonitrile (o-PAN) nanofibers and PAA chains, the o-PAN/PI (oPP) carbon aerogel exhibits a highly interconnected structure with plentiful carbon nanofibers supported between laminated carbon sheets, which results in tortuous pathways and an enhanced capillary effect for liquid storage. Therefore, the oPP carbon aerogel can be directly used not only as a versatile adsorbent for oil/organic pollutants, but also as a multi-dimensional support for the construction of a high-performance oPP@MnO_2 hybrid carbon aerogel electrode. As expected, an oPP@MnO_2//activated oPP (A-oPP) asymmetric supercapacitor exhibits a high energy density of 30.3 W h kg^{-1}, which exceeds that of most previously reported MnO_2-based asymmetric supercapacitors. The high performance of the oPP@MnO_2 hybrid carbon aerogel is ascribed to its uniformly anchored δ-phase MnO_2 nanosheets with a two-dimensional lamellar structure and interconnected 3D pathways consisting of 1D carbon nanofibers and 2D carbon sheets, which can not only enhance the surface adsorption ability of the MnO_2 nanosheets toward electrolytes but also increase the electron transfer rate inside electrode materials. Therefore, this work provides an innovative strategy for obtaining multi-dimensional carbon aerogels for versatile applications in the fields of environmental protection and highly efficient energy storage devices.

Experimental

Materials

Polyacrylonitrile (PAN, M_w = 150 000 g mol^{-1}) was purchased from Sigma-Aldrich. 4,4′-oxidianiline (ODA), pyromellitic dianhydride (PMDA), triethylamine (TEA, 98%), *N*,*N*-dimethylacetamide (DMAc), *N*,*N*-dimethylformamide (DMF), potassium permanganate ($KMnO_4$), cyclohexane, ethanol, acetone, benzyl alcohol, hexane, heptanes, isopropyl alcohol, octadecylene, toluene and chloroform were all purchased from Sinopharm Chemical Reagent Co. Commercially available oil products (*i.e.*, pump oil and colza oil) were used as probe liquids for studies of oil sorption capacity. All chemicals were of analytical grade and were used without further purification.

Preparation of o-PAN nanofiber membranes

The preparation process of o-PAN nanofiber membranes is similar to that in our previous work.[16] In brief, PAN powder was dissolved in DMF solvent under magnetic stirring for 6 h to form a transparent solution of PAN with a solid concentration of 10 wt%. The solution was loaded into a 5 mL plastic syringe capped with a metal needle having an inner diameter of 0.5 mm. A high voltage of 15 kV was applied to the needle tip to generate continuous jetting streams at a controllable feeding rate of 1 mL per hour. The resulting PAN nanofibers were collected by a grounded metallic rotating roller with a distance of 15 cm between the spinneret and the collector. After deposition for 45 min, a PAN nanofiber membrane was obtained and pre-oxidized at 250 °C for 2 h at a ramp rate of 2 °C min^{-1} to form an o-PAN nanofiber membrane.

Preparation of water-soluble poly(amide acid)-triethylamine (PAA-TEA) salt

Poly(amide acid) (PAA), the precursor of polyimide (PI), was synthesized in accordance with our previous work.[17] Typically, 8.62 g 4,4′-ODA was completely dissolved in 102 g DMAc solvent under vigorous stirring. Subsequently, 9.38 g PMDA was added and the mixture was stirred at 0 °C for 5 h. On the completion of polymerization, 4.36 g TEA was slowly dropped into the viscous fluid to form a water-soluble PAA solution. After the reaction, the obtained product was slowly dropped into deionized water, during which PAA-TEA salt was precipitated. After several precipitation processes and freeze-drying, fibrous PAA-TEA salt was obtained and stored for further use.

Preparation of o-PAN/PAA aerogel, o-PAN/PI aerogel, oPP carbon aerogel and activated oPP carbon aerogel

In a typical synthesis of the o-PAN/PAA-33.3 aerogel (where 33.3 refers to the mass percentage of PAA in the o-PAN/PAA composite aerogel), 2 g o-PAN nanofiber membrane was dispersed in a 100 mL aqueous solution (containing 1 g water-soluble PAA-TEA salt and 0.5 g TEA cosolvent) and homogenized at 18 000 rpm (using an IKA T25 homogenizer) for 30 min, yielding a uniform dispersion of o-PAN nanofibers in a PAA solution. A certain amount of the dispersion that was confined within various molds

was frozen by liquid nitrogen, and freeze-dried for 48 h to form the o-PAN/PAA-33.3 composite aerogel. In the same way, o-PAN/PAA composite aerogels with different o-PAN/PAA mass ratios (at a total solid content of 3 wt%) were denoted as o-PAN/PAA-0, o-PAN/PAA-16.7 and o-PAN/PAA-50 aerogels, respectively. Then, the o-PAN/PAA composite aerogels were heated to 300 °C under a nitrogen flow at a heating rate of 2 °C min^{-1}, during which they were kept at 100 °C, 200 °C, and 300 °C for 30 min, 30 min, and 60 min, respectively, to achieve sufficient imidization of PAA chains to polyimide, and named as o-PAN/PI-0, o-PAN/PI-16.7, o-PAN/PI-33.3 and o-PAN/PI-50 composite aerogels, respectively. Finally, the o-PAN/PI composite aerogels were heated to 800 °C at a ramp rate of 5 °C min^{-1} and kept for 1 h under a nitrogen flow. The resulting products were named as oPP-0, oPP-16.7, oPP-33.3, and oPP-50 carbon aerogels, respectively.

Furthermore, an activation process of the above carbon aerogels was carried out according to a previously reported work.[18] In brief, a physical mixture of the carbon aerogels and anhydrous KOH in a weight ratio of 1 : 4 was heated to 750 °C under a nitrogen flow at a heating rate of 10 °C min^{-1}, during which it was kept at 450 °C and 750 °C for 1 h and 4 h, respectively. The resulting materials were washed with 10% HCl solution and distilled water repeatedly to remove both potassium and chloride ions and finally dried at 110 °C for 6 h. The activated oPP-33.3 carbon material is denoted as A-oPP-33.3.

Preparation of oPP-33.3@MnO_2 hybrid carbon aerogel

The oPP-33.3 carbon aerogel was first immersed in concentrated sulfuric acid for 0.5 h to increase its hydrophilicity. Subsequently, 20 mg acid-treated oPP-33.3 carbon aerogel and 100 mg $KMnO_4$ were added together to 20 mL deionized water and the mixture was stirred for 0.5 h at room temperature, and then kept at 80 °C in an oil bath for 2 h. Finally, the as-prepared sample was washed with deionized water/alcohol several times and dried at 70 °C for 24 h to form the oPP-33.3@MnO_2-2 h hybrid carbon aerogel. In addition, a series of samples obtained after different redox reaction times (*i.e.*, 0.5 h, 1 h and 4 h) were named as oPP-33.3@MnO_2-0.5 h, oPP-33.3@MnO_2-1 h, and oPP-33.3@MnO_2-4 h hybrid carbon aerogels, respectively.

Characterization

Field emission scanning electron microscopy (FESEM, Ultra 55, Zeiss) was performed at an accelerating voltage of 5 kV. The chemical composition was investigated by energy-dispersive X-ray spectroscopy (EDS). Transmission electron microscopy (TEM) was carried out using a JEM-2100F field emission electron microscope at an accelerating voltage of 200 kV. Fourier transform infrared spectra (FT-IR) were recorded using a Nicolet 6700 spectrometer. X-ray diffraction (XRD) experiments were performed using a Philips X'Pert Pro Super diffractometer with Cu K_α radiation ($\lambda = 1.5418$ Å) at a speed of 5° min^{-1} from $2\theta =$ 10° to 70°. X-ray photoelectron spectroscopy (XPS) analyses were carried out on a RBD upgraded PHI-5000C ESCA system (Perkin-Elmer) with Mg K_α radiation ($h\nu = 1253.6$ eV). All XPS spectra were corrected using the C 1s line at 284.6 eV, whereas curve fitting and background subtraction were performed using RBD AugerScan 3.21 software. The mass percentage of MnO_2 in oPP@MnO_2 hybrid carbon aerogels was determined by thermogravimetric analysis (Pyris 1 TGA, Perkin-Elmer) under an air atmosphere from 100 to 700 °C at a heating rate of 20 °C min^{-1}.

Adsorption of oils and organic solvents by oPP carbon aerogels

In a typical adsorption experiment, a piece of carbon aerogel was directly placed in an organic liquid or oil until adsorption equilibrium was reached, and then taken out for measurement of its weight. The weight gain of the aerogel was calculated according to its change in weight before and after adsorption. In order to prevent the evaporation of adsorbed organic liquids with low boiling points, the measurement of weight was performed quickly. All adsorption experiments were conducted three times to determine the average adsorption capacity.

Electrochemical measurements

Electrodes that were used for electrochemical measurements were prepared by mixing an electroactive material, carbon black, and polytetrafluoroethylene in a mass ratio of 80 : 10 : 10 to obtain a homogeneous slurry. Then, the resulting slurry was coated onto nickel foam, dried at 80 °C for 12 h, and pressed at 10 MPa. The mass loading of active materials was fixed at 3 mg. For a standard three-electrode measurement, the working electrode tests were performed on an electrochemical working station (CHI660D, Chenhua Instruments Co. Ltd., Shanghai), where Ag/AgCl and Pt wire were used as the reference and counter electrode, respectively. Cyclic voltammograms (CV), galvanostatic charge–discharge (GCD) and electrochemical impedance spectroscopy (EIS) were employed to investigate the electrochemical properties of the active materials. The specific capacitance (C_s) of the electrode can be calculated from CV curves according to the following equation:

$$C_s = \frac{\int I \mathrm{d}V}{\nu m V} \quad (1)$$

where I is the current (A), ν is the potential scan rate (mV s^{-1}), V is the potential (V), and m is the mass of electroactive materials in the electrode (g).

An asymmetric supercapacitor was assembled using oPP-33.3@MnO_2 as the positive electrode material, A-oPP-33.3 as the negative electrode material, and filter paper as the separator, and tests were performed in an aqueous electrolyte solution of 1.0 M Na_2SO_4. The following equation was used to estimate the loading mass ratio of positive electrode material to negative electrode material:

$$\frac{m_+}{m_-} = \frac{C_- \times V_-}{C_+ \times V_+} \quad (2)$$

where m is the mass of the electrode material (g), C is the specific capacitance (F g^{-1}), and V is the potential (V).

The key parameters of the asymmetric supercapacitor, the power density (P) and energy density (E), were calculated according to the following equations:

$$E = \frac{1}{2} \times C \times V^2 \quad (3)$$

$$P = \frac{E}{\Delta t} \quad (4)$$

where E is the energy density (W h kg^{-1}), P is the power density (W kg^{-1}), C is the specific capacitance (F g^{-1}), V is the potential (V), and Δt is the discharge time (s) according to the galvanostatic charge–discharge curves.[19–21]

Results and discussion

As shown in Fig. 1a, an electrospun polyacrylonitrile (PAN) nanofiber (Fig. S1†) membrane was selected as the skeleton component and oxidized to increase its hydrophilicity by incorporating oxygen-containing functional groups such as –OH and –NH_2.[22,23] Thus, water-soluble poly(amide acid) (PAA) chains were easier to integrate with hydrophilic oxidized polyacrylonitrile (o-PAN) nanofibers under high-speed homogenization to form a homogeneous dispersion. After freeze-shaping, imidization and carbonization processes, well-shaped o-PAN/PI (oPP) carbon aerogels with various o-PAN/PAA mass ratios were obtained. As shown in Fig. S2a,† the macroscopic oPP-0 carbon aerogel is composed of randomly stacked as-collected carbon nanofibers with a disordered 3D fibrous structure, exhibiting poor mechanical properties (Fig. 1b) owing to the lack of both chemical and physical bonds. By adding a small amount of PAA to the o-PAN-based fibrous system to obtain oPP-16.7 carbon aerogels (Fig. S2b†), sparse polyimide-derived carbon sheets were produced among the carbon nanofibers, which provided a limited improvement in the structural stability. In contrast, the carbon nanofibers were excessively wrapped by polyimide-based carbon sheets when the mass fraction of PAA was further increased to 50% (Fig. S2c†), which severely limited the porous characteristics. In particular, the oPP-33.3 carbon aerogel with an appropriate mass fraction of PAA consists of one-dimensional (1D) carbon nanofibers and two-dimensional (2D) carbon sheets, displaying a distinct open-cell geometry with a cellular pore size distribution around 5–20 μm (Fig. 1c and S2d†). In contrast to the traditional fibrous carbon aerogels,[24] the unique structure of the oPP-33.3 carbon aerogel with plentiful carbon nanofibers supported between laminated carbon sheets endows it with outstanding bearing capacity (over 500 times its own weight), which is superior to the poor mechanical properties of oPP-0 carbon aerogels, as shown in Fig. 1b. Moreover, the free volume of the oPP-33.3 carbon aerogel with its cellular structure is fully occupied by air, leading to its ultralow density, which allows it to stand on the seedhead of a dandelion (Fig. 1d).

A more detailed TEM image (Fig. 2a) reveals that ultrathin carbon sheets are wrapped on the surface of carbon nanofibers and extended to form bridges with each other inside the oPP-33.3 carbon aerogel. Actually, the formation process of the oPP-33.3 carbon aerogel is proposed to occur *via* a three-step transformation, as shown in Fig. 2b. (1) Certain amounts of –OH and –NH_2 are formed on the surface of o-PAN nanofibers owing to the uptake of oxygen and evolution of gases (*e.g.*, NH_3, which is derived from the slight decomposition of nitrile groups) after pre-oxidation.[25–27] During the homogenization process, the hydrophilic –OH and –NH_2 groups of o-PAN nanofibers act as 'fishing rods' to adsorb PAA chains through strong hydrogen bonds between –COOH and –OH/–NH_2 groups. Therefore, the peak intensity of the o-PAN/PAA-33.3 aerogel at 2245 cm^{-1}, which corresponds to the –C≡N groups of o-PAN chains (blue line, Fig. 2c) is weaker compared with that (black line, Fig. 2c) of the bulk o-PAN nanofiber membrane. (2) The formation of the five-membered imide ring of polyimide, with the appearance of typical peaks at 1780 cm^{-1}, 1720 cm^{-1}, 1378 cm^{-1} and 725 cm^{-1} (blue-green line), instead of those at 1660 cm^{-1} and 1550 cm^{-1} for PAA chains (red and blue lines),[28,29] results in strong π-electron interactions between approaching rings, which contributes to the rigid structure of o-PAN/PI-33.3 aerogels.[30] (3) The typical peaks of o-PAN/PI-33.3 are replaced by an obvious peak at 1625 cm^{-1} and a broad peak around 1150 cm^{-1}, which are ascribed to the C=C and C–N

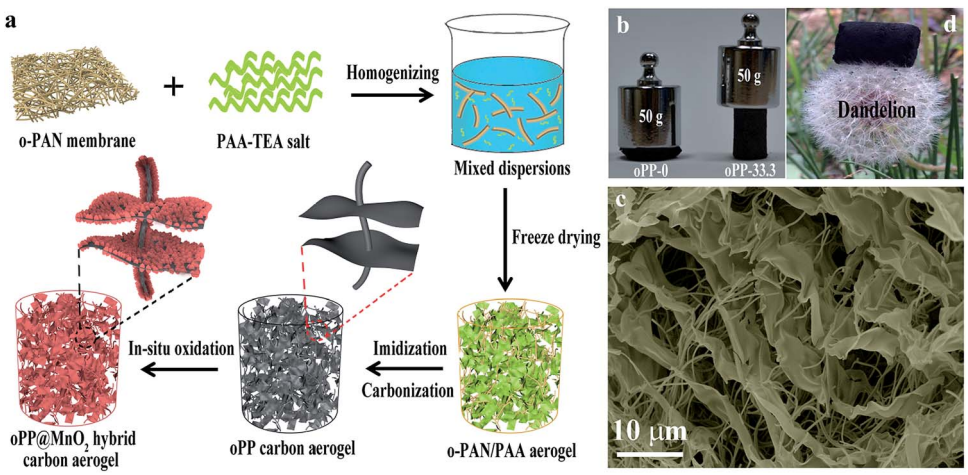

Fig. 1 (a) Schematic of the preparation of o-PAN/PAA aerogel, o-PAN/PI aerogel, oPP carbon aerogel, and oPP@MnO_2 hybrid carbon aerogel; (b) digital photograph for comparison of the stress tolerance between oPP-0 and oPP-33.3 carbon aerogels; (c) typical FESEM image of oPP-33.3 carbon aerogel; (d) digital photograph of oPP-33.3 carbon aerogel standing on a dandelion.

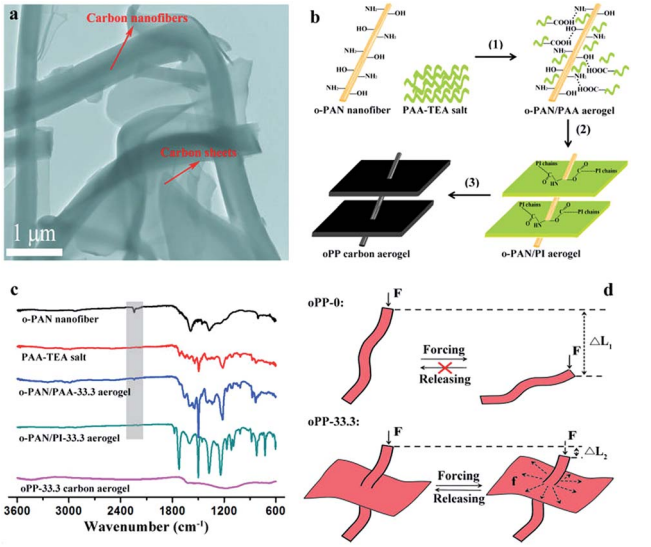

Fig. 2 (a) TEM image of oPP-33.3 carbon aerogel; (b) schematic illustration of the mechanism of the formation process of oPP-33.3 carbon aerogels; (c) FTIR spectra of o-PAN nanofibers, PAA-TEA salt, o-PAN/PAA-33.3 aerogel, o-PAN/PI-33.3 aerogel and oPP-33.3 carbon aerogel; (d) schematic illustration of the proposed mechanism for comparison between oPP-0 and oPP-33.3 carbon aerogels.

stretching vibrations of the oPP-33.3 carbon aerogel, respectively, which indicate the successful carbonization of the o-PAN/PI-33.3 aerogel and the removal of oxygen-containing functional groups. Therefore, the oPP-0 carbon aerogel is severely deformed with an obvious deformation of ΔL_1 under an external force ($\boldsymbol{F}$), which cannot be recovered even after the removal of $\boldsymbol{F}$ owing to the lack of effective chemical/physical bonds between the carbon nanofibers, whereas no evident structural compression ($\Delta L_2 \approx 0$) is observed for the oPP-33.3 carbon aerogel, as the external force is decomposed into multi-directional forces ($\boldsymbol{f}$) in the 2D plane of carbon sheets, where a hardened structure is generated by the rigid chains of polyimide, as illustrated in Fig. 2d. In consideration of its low density and extraordinary mechanical properties, the obtained oPP-33.3 carbon aerogel with its 3D porous structure is deemed to be a promising candidate for the removal of spilled oils and organic solvents in water (Fig. S3–S7†).

Interestingly, nitrogen doping is further demonstrated for the oPP-33.3 carbon aerogel *via* analysis of its surface information (Fig. S8a†), with three well-fitted peaks centered at 398.0, 399.8, and 401.1 eV in the high-resolution N 1s XPS spectrum (Fig. S8b†) that correspond to pyridinic, pyrrolic, and graphitic nitrogens, respectively, which indicates the potential value of the oPP-33.3 carbon aerogel as an energy storage material. Furthermore, chemical activation is reported to be a valid method for enhancing the electrical double-layer capacitive properties of carbon materials by introducing porous structures and generating more active sites for ion adsorption.[31,32] As was expected, the resulting electrochemical capacity of an activated oPP-33.3 carbon aerogel (A-oPP-33.3) electrode is 1.5 times higher than that of an oPP-33.3 carbon aerogel electrode (Fig. S9†). Owing to its 3D porous structure for efficient ion diffusion/adsorption and interconnected conductive network for electron transport, the cyclic voltammogram (CV) of the A-oPP-33.3 carbon aerogel exhibits good retention of its rectangular shape even at a high scan rate of 200 mV s^{-1} (shown in Fig. 3a), which indicates its excellent electrical double-layer capacitive performance. Likewise, the outstanding properties of the A-oPP-33.3 carbon aerogel can also be observed from its galvanostatic charge–discharge curves, which have linear and symmetrical shapes, as shown in Fig. 3b, further confirming its rapid ion adsorption rate during electrochemical processes. Besides, the low resistance of the A-oPP-33.3 carbon aerogel electrode can be demonstrated from its inconspicuous IR drop (IR_{drop} [V] = 0.0012 + 0.0024 [A g^{-1}]), as shown in Fig. 3b, with the corresponding quantitative analysis shown in Fig. S10.† In contrast to the limited capacitive properties of the oPP-33.3 carbon aerogel, the maximum specific capacitance of the A-oPP-33.3 carbon aerogel reaches 307.2 F g^{-1} at a scan rate of 2 mV s^{-1}, which is comparable to previously reported values for carbon-based electrode materials such as bacterial cellulose/lignin-based carbon aerogels (124 F g^{-1}, 0.5 A g^{-1}),[33] activated carbon nanofibers (296 F g^{-1}, 2 mV s^{-1}),[34] and nitrogen-doped graphene aerogels (223 F g^{-1}, 0.2 A g^{-1}).[35] Even at a high scan rate of 200 mV s^{-1}, the A-oPP-33.3 carbon aerogel displays a high retention of specific capacitance of 69.4% (213.1 F g^{-1} at 200 mV s^{-1}), which suggests its excellent rate stability at high current densities (Fig. 3c). Moreover, cycling stability is another important criterion for the commercial use of carbon-based double-layer capacitor materials. As shown in Fig. 3d, the capacitance of the A-oPP-33.3 carbon aerogel electrode displays a high retention of 96.3% with little variation in the CV curves after 5000 cycles at a scan rate of 100 mV s^{-1}, which suggests its remarkable cycling stability.

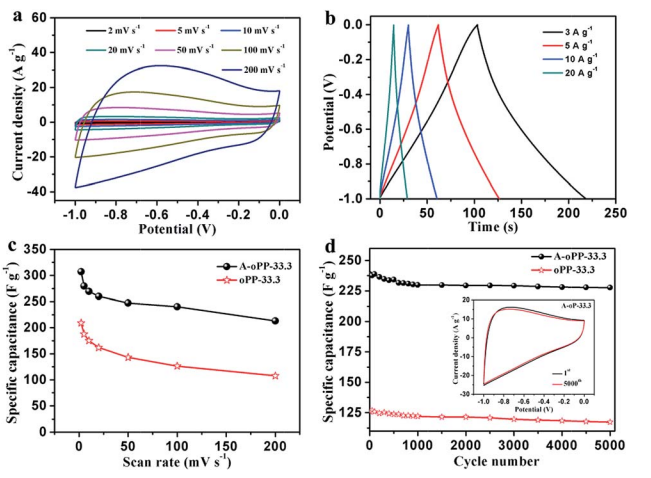

Fig. 3 Electrochemical tests on negative electrodes in an aqueous solution of 6.0 M KOH using a three-electrode system: (a) CV curves of the A-oPP-33.3 carbon aerogel at different scan rates ranging from 2 to 200 mV s^{-1}; (b) galvanostatic charge–discharge curves of the A-oPP-33.3 carbon aerogel at various current rates; (c) comparison of the specific capacitance between A-oPP-33.3 and oPP-33.3 carbon aerogels at different scan rates; (d) cycling stabilities of A-oPP-33.3 and oPP-33.3 carbon aerogels at a constant scan rate of 100 mV s^{-1} (the inset shows the CV curves for the 1st and 5000th cycles).

In the case of the unique multi-dimensional structure of the oPP-33.3 carbon aerogel, it is further considered to be an ideal template for the decoration of various pseudocapacitive nanoparticles to form hybrid electrode materials with superior electrochemical performance. Here, MnO_2 nanosheets were grown on the surface of an oPP-33.3 carbon aerogel template *via* an *in situ* oxidation reaction as follows:

$$4KMnO_4 + 3C + H_2O \rightarrow 4MnO_2 + 2KHCO_3 + K_2CO_3$$

As shown in Fig. 4a and b and S11,† the 3D interconnected structure is well maintained after coverage by MnO_2 nanosheets in the oPP-33.3@MnO_2-2 h hybrid carbon aerogel, where MnO_2 nanosheets were homogeneously deposited on the surface of both carbon nanofibers and carbon sheets without obvious self-agglomeration, which demonstrates high stability of the carbon aerogel template during the *in situ* oxidation process. The corresponding energy-dispersive X-ray spectroscopy (EDS) elemental mappings (Fig. 4c–f) and spectrum (Fig. S12†) further confirm the uniform growth of MnO_2 nanosheets on the surface of the oPP-33.3 carbon aerogel template. In addition, oPP-33.3@MnO_2-*x* h hybrid carbon aerogels with different thicknesses of MnO_2 nanosheets (where $x = 0.5$, 1, and 4, respectively) were also obtained by controlling the deposition time (Fig. S13†), which resulted in different mass loadings of MnO_2 nanosheets for the various oPP-33.3@MnO_2-*x* h hybrid carbon aerogels, as calculated from their TGA curves (Fig. S14 and Table S2†). Furthermore, it is worth noting that the diameter of carbon nanofibers for oPP-33.3@MnO_2-2 h increased to ~400 nm after the redox reaction, which indicates that the thickness of the MnO_2 layers is about 100 nm (Fig. 4g). Moreover, the XRD patterns (Fig. S15†) suggest that the crystal form of the MnO_2 nanosheets on the carbon aerogel template is birnessite-type (δ-MnO_2) (JCPDS no. 80-1098)[36] with an interlayer distance of 0.73 nm, which can effectively enhance the electrochemical properties of oPP-33.3@MnO_2-*x* h hybrid carbon aerogels, whereas the XPS spectrum (Fig. S16†) presents a clear identification of its oxidation state with no Mn^{2+} species.

Then, the electrochemical performance of oPP-33.3@MnO_2-*x* h hybrid carbon aerogels was evaluated in an aqueous electrolyte of 1.0 M Na_2SO_4 with a three-electrode system. Rectangular CV curves are observed for the oPP-33.3@MnO_2-0.5, 1, and 2 h hybrid carbon aerogels in Fig. 5a, which indicates their excellent rate stability. However, the low current density achieved for the oPP-33.3@MnO_2-4 h hybrid carbon aerogel indicates its poor energy storage properties, owing to the excessive growth of MnO_2 nanosheets, which limit the electron/electrolyte transfer rate at a high scan rate. Among these, the oPP-33.3@MnO_2-2 h hybrid carbon aerogel exhibits the CV curve with the largest proportions, which results in an optimal specific capacitance of 202.9 F g^{-1} at a scan rate of 50 mV s^{-1} (Fig. S17†). Specifically, the charge–discharge behavior of the oPP-33.3@MnO_2-2 h hybrid carbon aerogel at various discharge rates is shown in Fig. 5b, with symmetric shapes and constant slopes that prove its ideal capacitive performance as a supercapacitor electrode. In particular, excellent rate stability is also an important target to meet the practical requirements for

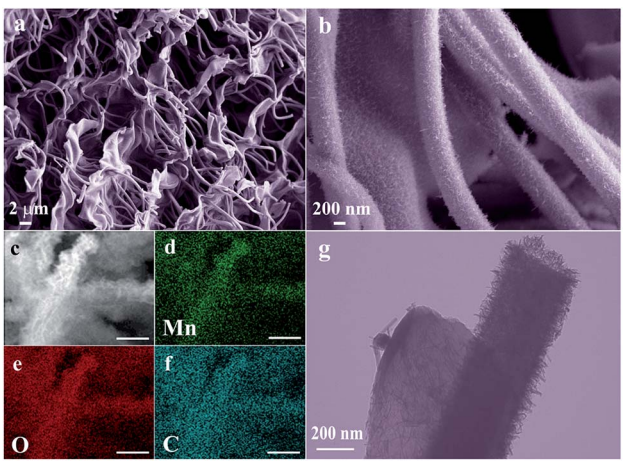

Fig. 4 Low- (a) and high-magnification (b) FESEM images of oPP-33.3@MnO_2-2 h hybrid carbon aerogel; corresponding EDS elemental mappings (c–f; the scale bars are 2.5 μm) of oPP-33.3@MnO_2-2 h hybrid carbon aerogel: (d) Mn, (e) O, (f) C; (g) TEM image of oPP-33.3@MnO_2-2 h hybrid carbon aerogel.

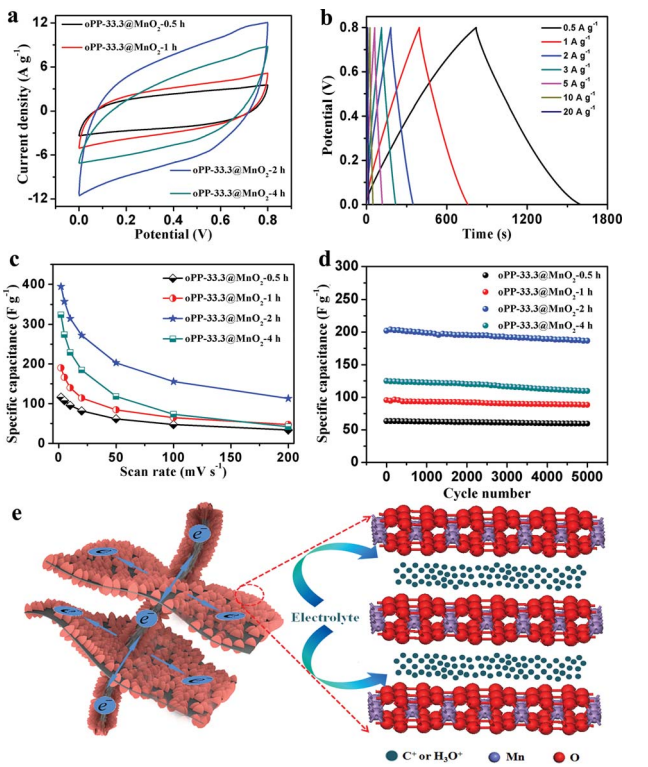

Fig. 5 Electrochemical tests on the positive electrodes in an electrolyte of 1.0 M Na_2SO_4 using a three-electrode system: (a) CV curves for oPP-33.3@MnO_2-*x* h hybrid carbon aerogels at a scan rate of 50 mV s^{-1} (where $x = 0.5$, 1, 2, and 4, respectively); (b) galvanostatic charge–discharge curves of the oPP-33.3@MnO_2-2 h hybrid carbon aerogel at various current rates; (c) rate stability of oPP-33.3@MnO_2-*x* h hybrid carbon aerogels at various scan rates; (d) cycling stability of oPP-33.3@MnO_2-*x* h hybrid carbon aerogels at a scan rate of 50 mV s^{-1}; (e) illustration of the electrolyte/electron transport pathways in the oPP-33.3@MnO_2-*x* h hybrid carbon aerogels.

supercapacitor electrodes at high scan rates. In Fig. 5c, the oPP-33.3@MnO_2-2 h hybrid carbon aerogel exhibits a maximum specific capacitance of 394.4 F g^{-1} at a scan rate of 2 mV s^{-1}, *i.e.*, 1066 F g^{-1} based on active MnO_2, which approaches its theoretical capacitance of 1370 F g^{-1}.[37] Furthermore, a high capacitance of 113.2 F g^{-1} can still be achieved for the oPP-33.3@MnO_2-2 h hybrid carbon aerogel even at a scan rate of 200 mV s^{-1}, which is much greater than those of other composites. Moreover, the oPP-33.3@MnO_2-2 h hybrid carbon aerogel also exhibits a high retention of 92.4% after 5000 cycles (Fig. 5d), which indicates its outstanding long cycling stability. The extraordinary performance in both rate and cycling stability of the oPP-33.3@MnO_2-2 h hybrid carbon aerogel can be ascribed to three aspects, as illustrated in Fig. 5e: (1) firstly, the uniform decoration of MnO_2 nanosheets effectively prevents their self-agglomeration and dramatically increases the specific surface area to achieve better contact between the electroactive materials and the electrolytes; (2) secondly, the 2D lamellar structure of δ-phase MnO_2 nanosheets with an interlayer distance of 0.73 nm is beneficial for maximizing both the pseudocapacitance behavior in electrochemical reactions and the surface adsorption of electrolyte cations (such as K^+ and Na^+);[38,39] (3) thirdly, the interconnected 3D pathways consisting of carbon nanofibers and carbon sheets under the coverage of MnO_2 nanosheets significantly increase the electron transfer rate inside the electrode materials.

An asymmetric supercapacitor was assembled by using the A-oPP-33.3 carbon aerogel as the negative electrode and the oPP-33.3@MnO_2 hybrid carbon aerogel as the positive electrode, respectively, and was denoted as the oPP-33.3@MnO_2-*x* h//A-oPP-33.3 asymmetric supercapacitor (ASC) device (Fig. 6a and Fig. S18†). As shown in Fig. 6b, the stable potential ranges are −1.0 to 0 V for the A-oPP-33.3 carbon aerogel electrode and 0–0.8 V for the oPP-33.3@MnO_2-2 h hybrid carbon aerogel electrode, respectively, leading to a greatly extended range of operating cell voltage for the oPP-33.3@MnO_2-2h//A-oPP-33.3 ASC device. The assembled ASC device exhibits good capacitive behavior, which is reflected by its nearly rectangular CV curves in different potential windows (Fig. 6c). In particular, the detailed properties, including the CV curves, rate stability, and flexibility, of the assembled ASC device are shown in Fig. S20 and S21.† In addition, the ASC device exhibits excellent cycling performance, as shown in Fig. 6d, with a capacitance retention of 92% after 2000 cycles at a constant scan rate of 50 mV s^{-1}. The energy densities and power densities for the oPP-33.3@MnO_2-2 h//A-oPP-33.3 ASC at various current densities are shown in a Ragone plot (Fig. 6e), which shows that it delivers a maximum energy density of 30.3 W h kg^{-1} at a power density of 501.3 W kg^{-1}. Such an excellent electrochemical performance is much better than that of most previously reported MnO_2-based asymmetric/symmetric supercapacitors such as MnO_2//CNT (10.3 W h kg^{-1}),[40] activated carbon//MnO_2/CNTs (13.3 W h kg^{-1}),[41] graphene hydrogel//MnO_2-nickel foam (23.2 W h kg^{-1}),[42] MnO_2/$MnCO_3$/rGO//rGO (17.8 W h kg^{-1}),[43] graphene/MnO_2/CNTs//graphene/MnO_2/CNTs (3.2 W h kg^{-1}),[44] graphene/MnO_2//graphene/MnO_2 (6.8 W h kg^{-1}),[45] and MnO_2 nanowire/graphene//graphene (7.0 W h kg^{-1}).[46] Therefore, the asymmetric supercapacitor based on the oPP-33.3 carbon aerogel and oPP-33.3@MnO_2-2 h hybrid carbon aerogel with its outstanding electrochemical performance suggests potential applications in high-performance energy storage devices.

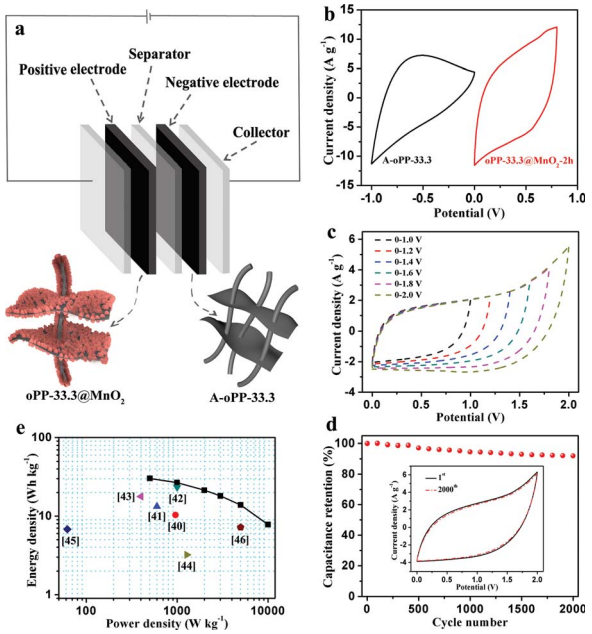

Fig. 6 (a) Schematic of the assembled asymmetric supercapacitor based on oPP-33.3@MnO_2-*x* h hybrid carbon aerogels as the positive electrode and A-oPP-33.3 as the negative electrode; (b) comparative CV curves for oPP-33.3@MnO_2-2 h hybrid carbon aerogel and A-oPP-33.3 carbon aerogel electrodes in a three-electrode setup in a solution of 1.0 M Na_2SO_4 at a scan rate of 50 mV s^{-1}; (c) CV curves of the oPP-33.3@MnO_2//A-oPP-33.3 asymmetric supercapacitor within different ranges of operating voltage at a scan rate of 50 mV s^{-1}; (d) cycling performance of the oPP-33.3@MnO_2//A-oPP-33.3 asymmetric supercapacitor at a constant scan rate of 50 mV s^{-1} (the inset shows the CV curves for the 1st and 2000th cycles); (e) Ragone plot for the oPP-33.3@MnO_2//A-oPP-33.3 asymmetric supercapacitor with recently reported values for comparison.

Conclusions and outlook

In summary, o-PAN/PI (oPP) carbon aerogels consisting of one-dimensional carbon nanofibers and two-dimensional carbon sheets derived from oxidized polyacrylonitrile (o-PAN) nanofibers and polyimide (PI), respectively, have been successfully obtained by combining electrospinning, freeze-shaping and carbonization processes. Benefiting from their multi-dimensional structure and enhanced capillary effect, the oPP carbon aerogels have been employed as efficient versatile adsorbents for various pollutants, displaying high adsorption capacity and excellent recyclability. Interestingly, the porous structure of the oPP carbon aerogel makes it an outstanding template for further decoration with MnO_2 nanoparticles to produce high-performance electrode materials, as well as the precursors of activated oPP (A-oPP) carbon materials. Here, the assembled oPP@MnO_2//A-oPP asymmetric supercapacitor exhibits a high energy density of 30.3 W h kg^{-1} at a power density of 501.3 W kg^{-1} in an

electrolyte of 1.0 M Na_2SO_4, which is much higher than most of the previously reported values for MnO_2-based asymmetric supercapacitors. The high performance of oPP@MnO_2 hybrid carbon aerogels is attributed to their uniformly anchored δ-phase MnO_2 nanosheets with a two-dimensional lamellar structure, together with their interconnected 3D pathways consisting of carbon nanofibers and carbon sheets, which can not only increase the surface adsorption ability of MnO_2 nanosheets toward electrolytes but also increase the electron transfer rate inside the electrode materials. Hence, this work provides a novel strategy for constructing multi-dimensional materials based on carbon aerogels with versatile applications as adsorbents and supercapacitor electrodes, which will dramatically widen the scope of two-dimensional electrospun nanofiber membranes to three-dimensional fibrous aerogels.

Acknowledgements

The authors are grateful for the financial support from the National Natural Science Foundation of China (51125011, 51373037, 51433001).

References

1 L. Sorensen, G. F. Strouse and A. E. Stiegman, *Adv. Mater.*, 2006, **18**, 1965–1967.
2 H. Y. Sun, Z. Xu and C. Gao, *Adv. Mater.*, 2013, **25**, 2554–2560.
3 M. E. Suss, T. F. Baumann, W. L. Bourcier, C. M. Spadaccini, K. A. Rose, J. G. Santiago and M. Stadermann, *Energy Environ. Sci.*, 2012, **5**, 9511–9519.
4 Z. Y. Wu, H. W. Liang, L. F. Chen, B. C. Hu and S. H. Yu, *Acc. Chem. Res.*, 2016, **49**, 96–105.
5 J. Li, X. Y. Wang, Q. H. Huang, S. Gamboa and P. J. Sebastian, *J. Power Sources*, 2006, **158**, 784–788.
6 S. A. Al-Muhtaseb and J. A. Ritter, *Adv. Mater.*, 2003, **15**, 101–114.
7 H. Tamon, H. Ishizaka, M. Mikami and M. Okazaki, *Carbon*, 1997, **35**, 791–796.
8 P. Lv, X. W. Tan, K. H. Yu, R. L. Zheng, J. J. Zheng and W. Wei, *Carbon*, 2016, **99**, 222–228.
9 S. A. Steiner, T. F. Baumann, B. C. Bayer, R. Blume, M. A. Worsley, W. J. MoberlyChan, E. L. Shaw, R. Schloegl, A. J. Hart, S. Hofmann and B. L. Wardle, *J. Am. Chem. Soc.*, 2009, **131**, 12144–12154.
10 P. S. Kumar, J. Sundaramurthy, S. Sundarrajan, V. J. Babu, G. Singh, S. I. Allakhverdiev and S. Ramakrishna, *Energy Environ. Sci.*, 2014, **7**, 3192–3222.
11 A. Greiner and J. H. Wendorff, *Angew. Chem., Int. Ed.*, 2007, **46**, 5670–5703.
12 F. L. Lai, Y. E. Miao, Y. P. Huang, T. S. Chung and T. X. Liu, *J. Phys. Chem. C*, 2015, **119**, 13442–13450.
13 G. G. Duan, S. H. Jiang, V. Jérôme, J. H. Wendorff, A. Fathi, J. Uhm, V. Altstädt, M. Herling, J. Breu, R. Freitag, S. Agarwal and A. Greiner, *Adv. Funct. Mater.*, 2015, **25**, 2850–2856.
14 G. G. Duan, S. H. Jiang, T. Moss, S. Agarwal and A. Greiner, *Polym. Chem.*, 2016, **7**, 2759–2764.
15 Y. Si, J. Y. Yu, X. M. Tang, J. L. Ge and B. Ding, *Nat. Commun.*, 2014, **5**, 5802–5810.
16 F. L. Lai, Y. P. Huang, Y. E. Miao and T. X. Liu, *Electrochim. Acta*, 2015, **174**, 456–463.
17 F. L. Lai, Y. E. Miao, L. Z. Zuo, Y. F. Zhang and T. X. Liu, *ChemNanoMat*, 2016, **2**, 212–219.
18 Y. W. Zhu, S. Murali, M. D. Stoller, K. J. Ganesh, W. W. Cai, P. J. Ferreira, A. Pirkle, R. M. Wallace, K. A. Cychosz, M. Thommes, D. Su, E. A. Stach and R. S. Ruoff, *Science*, 2011, **332**, 1537–1541.
19 H. Pang, Y. Z. Zhang, W. Y. Lai, Z. Hu and W. Huang, *Nano Energy*, 2015, **15**, 303–312.
20 H. Pang, Y. Z. Zhang, Z. Run, W. Y. Lai and W. Huang, *Nano Energy*, 2015, **17**, 339–347.
21 B. Li, M. B. Zheng, H. G. Xue and H. Pang, *Inorg. Chem. Front.*, 2016, **3**, 175–202.
22 P. Bajaj and A. K. Roopanwal, *J. Macromol. Sci., Rev. Macromol. Chem. Phys.*, 1997, **C37**, 97–147.
23 S. Soulis and J. Simitzis, *Polym. Int.*, 2005, **54**, 1474–1483.
24 S. D. Yang, L. Chen, L. Mu, B. Hao and P. C. Ma, *RSC Adv.*, 2015, **5**, 38470–38478.
25 J. C. Simitzis and P. C. Georgiou, *J. Mater. Sci.*, 2015, **50**, 4547–4564.
26 W. J. Burlant and J. L. Parsons, *J. Polym. Sci.*, 1956, **22**, 249–256.
27 S. K. Nataraj, K. S. Yang and T. M. Aminabhavi, *Prog. Polym. Sci.*, 2012, **37**, 487–513.
28 Q. Wu, W. Huang, H. J. Wang, L. L. Pan, C. L. Zhang and X. K. Liu, *Chin. J. Polym. Sci.*, 2015, **33**, 1125–1132.
29 J. Dong, C. Q. Yin, Z. X. Zhang, X. Y. Wang, H. B. Li and Q. H. Zhang, *Macromol. Mater. Eng.*, 2014, **299**, 1170–1179.
30 Y. C. Xiao, B. T. Low, S. S. Hosseini, T. S. Chung and D. R. Paul, *Prog. Polym. Sci.*, 2009, **34**, 561–580.
31 Y. P. Zhai, Y. Q. Dou, D. Y. Zhao, P. F. Fulvio, R. T. Mayes and S. Dai, *Adv. Mater.*, 2011, **23**, 4828–4850.
32 Y. Y. Lv, F. Zhang, Y. Q. Dou, Y. P. Zhai, J. X. Wang, H. J. Liu, Y. Y. Xia, B. Tu and D. Y. Zhao, *J. Mater. Chem.*, 2012, **22**, 93–99.
33 X. Z. Xu, J. Zhou, D. H. Nagaraju, L. Jiang, V. R. Marinov, G. Lubineau, H. N. Alshareef and M. Oh, *Adv. Funct. Mater.*, 2015, **25**, 3193–3202.
34 C. L. Long, D. P. Qi, T. Wei, J. Yan, L. L. Jiang and Z. J. Fan, *Adv. Funct. Mater.*, 2014, **24**, 3953–3961.
35 Z. Y. Sui, Y. N. Meng, P. W. Xiao, Z. Q. Zhao, Z. X. Wei and B. H. Han, *ACS Appl. Mater. Interfaces*, 2015, **7**, 1431–1438.
36 J. T. Hou, Y. Z. Li, M. Y. Mao, L. Ren and X. J. Zhao, *ACS Appl. Mater. Interfaces*, 2014, **6**, 14981–14987.
37 J. F. Zang and X. D. Li, *J. Mater. Chem.*, 2011, **21**, 10965–10969.
38 M. Toupin, T. Brousse and D. Belanger, *Chem. Mater.*, 2004, **16**, 3184–3190.
39 P. Simon and Y. Gogotsi, *Nat. Mater.*, 2008, **7**, 845–854.
40 C. C. Liu, D. S. Tsai, W. H. Chung, K. W. Li, K. Y. Lee and Y. S. Huang, *J. Power Sources*, 2011, **196**, 5761–5768.
41 L. Li, Z. A. Hu, N. An, Y. Y. Yang, Z. M. Li and H. Y. Wu, *J. Phys. Chem. C*, 2014, **118**, 22865–22872.

42 H. C. Gao, F. Xiao, C. B. Ching and H. W. Duan, *ACS Appl. Mater. Interfaces*, 2012, **4**, 2801–2810.
43 Y. C. Liu, D. W. He, H. L. Wu, J. H. Duan and Y. N. Zhang, *Electrochim. Acta*, 2015, **164**, 154–162.
44 Y. W. Cheng, S. T. Lu, H. B. Zhang, C. V. Varanasi and J. Liu, *Nano Lett.*, 2012, **12**, 4206–4211.
45 Y. M. He, W. J. Chen, X. D. Li, Z. X. Zhang, J. C. Fu, C. H. Zhao and E. Q. Xie, *ACS Nano*, 2013, **7**, 174–182.
46 Z. S. Wu, W. C. Ren, D. W. Wang, F. Li, B. L. Liu and H. M. Cheng, *ACS Nano*, 2010, **4**, 5835–5842.